



Time-resolved spatial structure of TEA CO₂ laser pulses

C. MARTÍNEZ, J. SERNA, F. ENCINAS-SANZ,
R. MARTÍNEZ-HERRERO AND P. M. MEJÍAS

Departamento de Óptica, Facultad de Ciencias Físicas, Universidad Complutense, 28040 Madrid, Spain
(E-mail: *fiopt01@sis.ucm.es*)

Received 4 January 1999; accepted 16 February 1999

Abstract. The evolution of the intensity profile of TEA CO₂ laser pulses along the pulse length is investigated both analytically and experimentally. A simple scalar model of the pulse amplitude is introduced, which gives the loaded-cavity modes as a linear combination of bidimensional Hermite–Gauss functions. According to this model a number of equations are derived which link the time-varying spatial structure of the pulse to its time-resolved second-order intensity moments, namely, the beam width and the M^2 parameter.

Key words: bidimensional characterization, electro-optical switch, Hermite–Gauss modes, laser pulses, TEA CO₂ laser

1. Introduction

As is well known, the spatial profile of a laser pulse cannot be expected, *a priori*, to remain constant along the pulse duration. In this connection, the time evolution of the transversal structure of light pulses is receiving increasing attention in the literature (Caprara and Reali 1992; Omatsu and Kuroda 1992; Chang 1994; Perrone *et al.* 1995). To characterize such evolution, time-resolved spatial parameters were defined (Mejías and Martínez-Herrero 1995; Morin *et al.* 1996) on the basis of the intensity moments formalism (Lavi *et al.* 1988; Bastiaans 1989; Siegman 1990; Serna *et al.* 1991; Weber 1992). Using this theory, the time-varying beam quality factor M^2 (Siegman 1990) of TEA CO₂ laser pulses was recently investigated by Encinas-Sanz *et al.* (1998). In that paper attention was focused on both, the instant in which the presence of a particular laser mode begins to be significant, and the time interval during which the modes grow to reach a quasi-stationary spatial behaviour. However, no information was inferred about the detailed intensity distribution associated to each mode.

In the present paper we will proceed further into the above research. On the one hand, we show how the intensity moment formalism can provide useful information to determine the evolution of high quality (say $M^2 < 2$) laser pulses. On the other hand, we investigate the dynamics of the spatial

structure of the pulses emitted by TEA CO₂ lasers with low Fresnel number cavities. Thus, in the next section, after describing the optical arrangement used in the measurements, the instantaneous field profiles at different times along the pulse length are shown. The experimental results correspond to the pulses emitted by a TEA CO₂ laser device. In Section 3, from the application of a simple scalar model of laser pulse, the time-resolved transversal spatial structure of the beam is shown to be linked to the instantaneous values of its second order intensity moments, namely, the beam width and the M^2 parameter. Furthermore, the modes of the loaded laser cavity will be explicitly given as a combination of certain Hermite–Gauss functions. Finally, the main conclusions are summarized in Section 4.

2. Experimental results

As was mentioned in the introduction, we consider in this work the pulses emitted by a TEA CO₂ laser device. The laser cavity is half symmetric, with a curved mirror (radius of curvature 10 m) and a flat output mirror separated 112 cm. The gas mixture was CO₂:N₂:He with proportions 1:4:11. Inside the cavity we have placed an intracavity Brewster plate to obtain a linearly polarized beam, and an intracavity diaphragm (diameter 10 mm) close to the curved mirror to reduce the Fresnel number. The energy was $\simeq 0.5$ J per pulse, with a $\simeq 70$ ns gain switch peak followed by a $\simeq 2$ μ s tail (Encinas-Sanz *et al.* 1998).

The experimental set-up shown in Fig. 1 has been described in detail elsewhere (Encinas-Sanz *et al.* 1998). Here we only point out that the ensemble pyroelectric camera (Spiricon PYROCAM I), laser beam analyzer and computer provides the (squared) beam widths averaged during time-

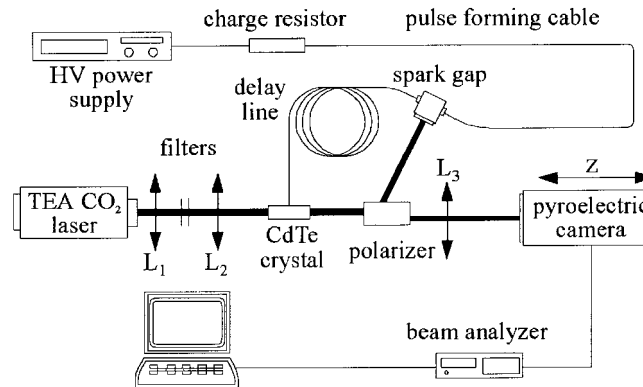


Fig. 1. Experimental set-up used for the measurements.

slices whose thickness ($\Delta t \simeq 10$ ns) is typically much shorter than the complete pulse duration. To cut such time-slices an electro-optical switching device based on a CdTe crystal and a polarizer was used. The system is triggered by the beam itself, using a spark gap that collects the rejected beam at the polarizer. The duration of the voltage pulse that defines the slice width is given by the length of the coaxial forming cable that links the spark gap and the high-voltage charge resistor, while the relative position of the time-slice within the laser pulse is controlled by the length of the delay cable between the spark gap and the switching device. Finally, the telescopic system formed by lenses L_1 and L_2 is used to avoid hard edge diffraction at the electro-optical crystal aperture. It reduces the beam size through the crystal, and maintains the energy density below the threshold damage level of the material. A third lens L_3 is used to generate a waist at the measurement region.

Using the above experimental arrangement, we have measured the (squared) beam width (second-order intensity moment) along, say, the x -axis, transversal to the propagation direction of the beam, z , for different time positions t_0 of the time-slice during the pulse evolution. The measured second-order moment $\langle x^2 \rangle$ is expressed in terms of the field amplitude f at plane z_0 in the form

$$\langle x^2 \rangle(z_0, t_0) = \frac{1}{H_{t_0}} \int_{t_0}^{t_0 + \Delta t} dt \int x^2 |f|^2 dx dy, \quad (1)$$

where $H_{t_0} = \int_{t_0}^{t_0 + \Delta t} dt \int |f|^2 dx dy$ is the total energy of the time-slice at t_0 , and $\Delta t \simeq 10$ ns is the FWHM temporal thickness of each time-slice. Note that, strictly speaking, we do not determine the instantaneous value of the beam size, but an average over a very short time interval Δt compared with the pulse duration.

The time-resolved bidimensional beam quality factor M^2 can be defined as follows

$$M^2(t_0) = \sqrt{4k^2 \langle x^2 \rangle_w \langle \theta^2 \rangle}, \quad (2)$$

where $k = 2\pi/\lambda$ ($\lambda = 10.6$ μm), the subscript w refers to the beam waist plane, and $\langle \theta^2 \rangle$ denotes the far-field divergence associated with the x variable, again integrated over the time interval Δt . For each time-slice, the values of $\langle x^2 \rangle$ measured versus propagation distance z_0 can be fitted to a parabolic curve, and from the parameters of the fitting parabola the value of the M^2 factor was easily inferred. Fig. 2 shows the contour images of the transversal spatial profile of the pulse, captured with the pyroelectric camera, at different times

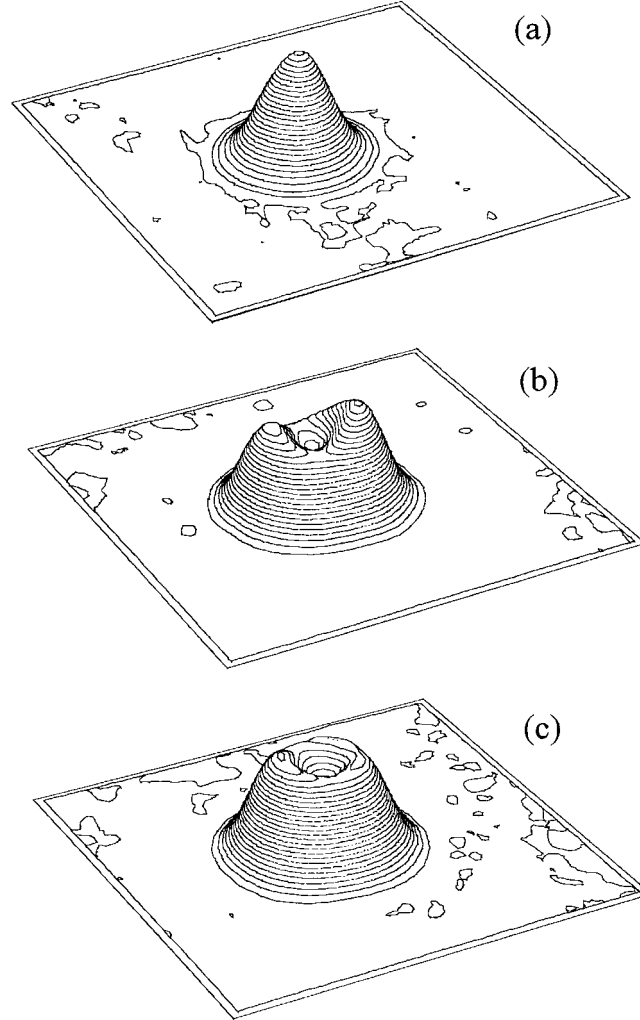


Fig. 2. Time resolved intensity profiles measured at different instants after the beginning of the pulse. (a) $t_0 = 25$ ns; (b) $t_0 = 400$ ns; (c) $t_0 = 600$ ns.

during the pulse evolution. The samples demonstrate that the time-varying structure exhibits three different behaviours: a first region at the beginning of the pulse ($t_0 < 100$ ns), in which the beam is nearly Gaussian and $M^2 \simeq 1.1$; a second region ($100 < t_0 < 500$ ns), in which M^2 increases to reach a value of about 1.9 and two intensity lobes appear with the orientation of these lobes changing from pulse to pulse; and a third region ($t_0 > 500$ ns) where M^2 is nearly constant ($M^2 \simeq 1.9$) and the pulse shows a doughnut-like profile.

To complete the experimental basis that will be used in the next section let us finally recall that the measurement of the so-called mode-beat, generated

by heterodyne interference effects at different frequencies between the modes, showed the presence of only one mode in the first region (Martínez *et al.* 1997). The same mode-beating experiments reveal the existence of two transversal modes in the second and third regions. Here we associate the term modes to definite spatial structures of the laser field, which resonate within the loaded cavity. The existence of different modes would then announce the presence of different transversal mode resonance frequencies.

3. Theory

Since at the leading edge of the pulse there is only one mode we will write the pulse amplitude ψ_a at the output plane of the laser cavity (waist plane of the beam) in the form

$$\psi_a(x, y, t) = \rho(t) \exp(i\omega_a t) \sum_n \sum_m B_{nm}(t) \varphi_n(x) \varphi_m(y), \quad (3)$$

where $\rho(t)$ denotes the temporal envelope of the pulse (which includes the information about the duration of the pulse), the exponential factor contains the rapid oscillations (ω_a is the angular frequency), and φ_n represents the Hermite–Gauss (H–G) functions, namely,

$$\varphi_p(x) = \beta_p H_p(\gamma x) \exp(-\gamma^2 x^2/2), \quad (4)$$

β_p being a constant, H_p the Hermite polynomials and γ another constant which is inferred from the geometry of the cavity (Siegman 1986; Martínez *et al.* 1997). In this region of the pulse ($t < 100$ ns) the M^2 parameter is nearly 1, and the intensity profile has axial symmetry. Therefore the spatial structure of the mode should be close (but not strictly equal) to a pure Gaussian amplitude. Accordingly, we will approach Equation (3) in the present case as follows

$$\begin{aligned} \psi_a(x, y, t) = \rho(t) \exp(i\omega_a t) \\ \times [B_{00}\varphi_0(x)\varphi_0(y) + B_{02}\varphi_0(x)\varphi_2(y) + B_{20}\varphi_2(x)\varphi_0(y)], \end{aligned} \quad (5)$$

where the coefficients must be coupled in such a way that ψ_a maintains its axial symmetry. This is why we have chosen the product of the even H–G functions φ_0 and φ_2 . Another fundamental reason for this choice will be given below.

It should be noted that the loaded cavity mode expressed in Equation (5) differs from the empty cavity modes given by single H–G functions. The same applies later in this section when we consider several transversal modes resonating inside the loaded cavity.

It can be shown that at each time-slice defined by t_0 the intensity moments (in the x variable) of the pulse given by Equation (5) are the same than those of a field whose correlation function is

$$\begin{aligned} \Gamma(x_1, x_2, t_0) &= \int_{t_0}^{t_0+\tau} \int_{-\infty}^{+\infty} \psi_a^*(x_1, y, t) \psi_a(x_2, y, t) dy dt \\ &= C_{00}^x \varphi_0(x_1) \varphi_0(x_2) + C_{02}^x \varphi_0(x_1) \varphi_2(x_2) \\ &\quad + C_{20}^x \varphi_2(x_1) \varphi_0(x_2) + C_{22}^x \varphi_2(x_1) \varphi_2(x_2), \end{aligned} \quad (6)$$

where

$$C_{00}^x = \int_{t_0}^{t_0+\tau} \rho^2(t) (|B_{00}|^2 + |B_{02}|^2) dt, \quad (7)$$

$$C_{02}^x = \int_{t_0}^{t_0+\tau} \rho^2(t) B_{00}^* B_{20} dt, \quad (8)$$

$$C_{20}^x = (C_{02}^x)^*, \quad (9)$$

$$C_{22}^x = \int_{t_0}^{t_0+\tau} \rho^2(t) |B_{20}|^2 dt. \quad (10)$$

In a similar way, it can be shown that the moments in the y variable of the pulse are identical to those of a field whose correlation function is

$$\begin{aligned} \Gamma(y_1, y_2, t_0) &= C_{00}^y \varphi_0(y_1) \varphi_0(y_2) + C_{02}^y \varphi_0(y_1) \varphi_2(y_2) \\ &\quad + C_{20}^y \varphi_2(y_1) \varphi_0(y_2) + C_{22}^y \varphi_2(y_1) \varphi_2(y_2), \end{aligned} \quad (11)$$

with

$$C_{00}^y = \int_{t_0}^{t_0+\tau} \rho^2(t) (|B_{00}|^2 + |B_{20}|^2) dt, \quad (12)$$

$$C_{02}^y = \int_{t_0}^{t_0+\tau} \rho^2(t) B_{00}^* B_{02} dt = (C_{20}^y)^*, \quad (13)$$

$$C_{22}^y = \int_{t_0}^{t_0+\tau} \rho^2(t) |B_{02}|^2 dt. \quad (14)$$

Let us now introduce the normalized coefficients R_{ij}^α , $i, j = 0, 2$, $\alpha = x, y$, defined as follows

$$R_{ij}^\alpha = \frac{C_{ij}^\alpha}{P}, \quad (15)$$

where P is proportional to the total energy per time-slice, i.e.,

$$P(t_0) = \sum_n C_{nn}^x = \sum_m C_{mm}^y. \quad (16)$$

It is important to note that, for the pulses analyzed in the measurements (in the region $t_0 < 100$ ns), no experimental difference exists between the spatial behaviour in the variables x and y . Accordingly, we will consider

$$R_{0j}^x = R_{0j}^y, \quad j = 0, 2. \quad (17)$$

From the recurrence properties of the H-G beams and their derivatives (Gradshteyn and Ryzhik 1986), it can be shown in a completely analogous way to that used by Martínez *et al.* (1997) that the following relations hold for a general pulse amplitude given by Equation (3):

$$0 = \sum_n (n+1)^{1/2} R_{n,n+1}^x, \quad (\text{centered beam}) \quad (18)$$

$$0 = \sum_n [(n+2)(n+1)]^{1/2} \text{Im}(R_{n,n+2}^x), \quad (\text{waist plane}) \quad (19)$$

$$r/2 = \sum_n [(n+2)(n+1)]^{1/2} \text{Re}(R_{n,n+2}^x), \quad (20)$$

$$a_x = \sum_n (2n+1) R_{nn}^x, \quad (21)$$

$$1 = \sum_n R_{nn}^x, \quad (22)$$

where

$$s \equiv 2\gamma^2 \langle x^2 \rangle, \quad (23)$$

$$r \equiv \frac{s^2 - M^2}{2s}, \quad (24)$$

$$a_x \equiv s - r. \quad (25)$$

In the above equations $\langle x^2 \rangle$ and M^2 are defined for each time-slice according to Equations (1) and (2), and are obtained directly from the experiment. Consequently, s and r should be considered as measurable quantities.

For the pulses we are analysing at present (see Equation (5)) the relations (18)–(22) reduce to

$$R_{00}^x = \frac{5 - a_x}{4} \simeq 0.95, \quad (26)$$

$$R_{02}^x = \frac{r}{2\sqrt{2}} = R_{20}^x \simeq -0.15, \quad (27)$$

$$R_{22}^x = 1 - R_{00}^x \simeq 0.05, \quad (28)$$

where the numerical values have been obtained from the experimental data. Due to the similar behaviour in the y -variable we have $R_{ij}^y = R_{ij}^x$, $i, j = 0, 2$.

It is important to remark that $r \neq 0$ for the pulses analysed here (see Equation (27)). According to Equation (20), this implies that the expression (3) should contain at least two H–G functions, which differ by two orders. This is consistent with the choice of the pulse amplitude given by Equation (5).

Taking all this into account, the intensity $I_a(x, y, t_0)$ in the first region of the pulse, where only one mode exists, can be expressed as the following superposition of bidimensional H–G functions:

$$\begin{aligned} \frac{I_a(x, y, t_0)}{P} &= r_{00} \varphi_0^2(x) \varphi_0^2(y) + r_{02} [\varphi_0^2(x) \varphi_2^2(y) + \varphi_2^2(x) \varphi_0^2(y)] \\ &\quad + 2\text{Re}(r_{00}^{(02)}) [\varphi_0^2(x) \varphi_0(y) \varphi_2(y) + \varphi_0(x) \varphi_2(x) \varphi_0^2(y)] \\ &\quad + 2\text{Re}(r_{02}^{(20)}) \varphi_0(x) \varphi_2(y) \varphi_2(x) \varphi_0(y), \end{aligned} \quad (29)$$

where

$$r_{00} = \int_{t_0}^{t_0+\tau} \rho^2 \frac{|B_{00}|^2}{P} dt = R_{00} - R_{22} = 0.90, \quad (30)$$

$$r_{02} = \int_{t_0}^{t_0+\tau} \rho^2 \frac{|B_{02}|^2}{P} dt = R_{22} = 0.05, \quad (31)$$

$$r_{00}^{(02)} = \int_{t_0}^{t_0+\tau} \rho^2 \frac{B_{00}^* B_{20}}{P} dt = R_{02} = -0.15, \quad (32)$$

$$r_{02}^{(20)} = \int_{t_0}^{t_0+\tau} \rho^2 \frac{B_{02}^* B_{20}}{P} dt = 0.05. \quad (33)$$

To write Equations (30)–(33) we have used Equations (26)–(28), along with the fact that the intensity profile of the pulse exhibits axial symmetry. Also note that the superscripts x, y have been omitted in the above equations to simplify the notation.

In summary, Equation (29) gives the time-resolved intensity at the beginning of the pulse at the resonator output plane. It should be remarked that we cannot infer from this expression the values of the (complex) coefficients B_{nm} (see Equation (3)). Consequently, the pulse amplitude cannot be determined. Also note that the pyroelectric camera used to collect the pulse profiles must be placed after the electro-optic switch. This prevents any direct intensity measurement at the output plane of the laser cavity.

Let us now consider the regions of the pulse in which mode-beating experiments show the presence of two transversal modes, ψ_a and ψ_b . This occurs for $t > 100$ ns. The pulse amplitude in this region will then be written in the form:

$$\psi(x, y, t) = \psi_a(x, y, t) + \psi_b(x, y, t) \quad (34)$$

with

$$\begin{aligned} \psi_a(x, y, t) = \rho(t) \exp(i\omega_a t) \\ \times \left[B_{00}^{(a)} \varphi_0(x) \varphi_0(y) + B_{02}^{(a)} \varphi_0(x) \varphi_2(y) + B_{20}^{(a)} \varphi_2(x) \varphi_0(y) \right], \end{aligned} \quad (35)$$

which is similar to Equation (5), and

$$\psi_b(x, y, t) = \rho(t) \exp(i\omega_b t) \left[B_{01}^{(b)} \varphi_0(x) \varphi_1(y) + B_{10}^{(b)} \varphi_1(x) \varphi_0(y) \right]. \quad (36)$$

The spatial structure of ψ_b has been chosen to fit the experimental data. In fact,

1. since the M^2 parameter remains smaller than 2, the contribution of H–G functions φ_n whose order n exceeds 2 should be considered as negligible;
2. for the time interval $100 < t_0 < 500$ ns, the intensity profile presents two lobes, whose orientation can change from one pulse to another. This behaviour can easily be explained using Equation (36): it would suffice that

$B_{10}^{(b)} = B_{01}^{(b)} \exp(i\delta)$, where $\delta \neq \pi/2$ is a constant phase factor, not determined a priori. If $\delta = \pi/2$, $|\psi_b|$ shows a doughnut shape, as occurs for $t > 500$ ns, when the pulse reaches a nearly stationary profile. This factor δ comes from a random phase which appears in the generation and growing process of the spatial structures $\varphi_0(x)\varphi_1(y)$ and $\varphi_1(x)\varphi_0(y)$ of the second mode.

Analogously to the previous case, when only one mode was present, it can be shown, after lengthy but straightforward calculations, that, at each time-slice, the intensity moments (in the x variable) of the pulse given by Equation (34) are identical to those of a field whose correlation function $\Gamma(x_1, x_2, t_0)$ is

$$\begin{aligned} \Gamma(x_1, x_2, t_0) = & R_{00}^x \varphi_0(x_1) \varphi_0(x_2) + R_{01}^x \varphi_0(x_1) \varphi_1(x_2) + R_{10}^x \varphi_1(x_1) \varphi_0(x_2) \\ & + R_{02}^x \varphi_0(x_1) \varphi_2(x_2) + R_{20}^x \varphi_2(x_1) \varphi_0(x_2) + R_{11}^x \varphi_1(x_1) \varphi_1(x_2) \\ & + R_{22}^x \varphi_2(x_1) \varphi_2(x_2) + R_{12}^x \varphi_1(x_1) \varphi_2(x_2) + R_{21}^x \varphi_2(x_1) \varphi_1(x_2), \end{aligned} \quad (37)$$

where

$$R_{00}^x = \frac{1}{P} \int_{t_0}^{t_0+\tau} \rho^2 (|B_{00}^{(a)}|^2 + |B_{02}^{(a)}|^2 + |B_{01}^{(b)}|^2) dt, \quad (38)$$

$$R_{01}^x = \frac{1}{P} \int_{t_0}^{t_0+\tau} \rho^2 \exp[i(\omega_b - \omega_a)t] (B_{00}^{(a)})^* B_{10}^{(b)} dt, \quad (39)$$

$$R_{02}^x = \frac{1}{P} \int_{t_0}^{t_0+\tau} \rho^2 (B_{00}^{(a)})^* B_{20}^{(a)} dt, \quad (40)$$

$$R_{11}^x = \frac{1}{P} \int_{t_0}^{t_0+\tau} \rho^2 |B_{01}^{(b)}|^2 dt, \quad (41)$$

$$R_{12}^x = \frac{1}{P} \int_{t_0}^{t_0+\tau} \rho^2 \exp[-i(\omega_b - \omega_a)t] B_{20}^{(a)} (B_{10}^{(b)})^* dt, \quad (42)$$

$$R_{22}^x = \frac{1}{P} \int_{t_0}^{t_0+\tau} \rho^2 |B_{20}^{(a)}|^2 dt. \quad (43)$$

In these formulas the integration in t is performed within the temporal thickness of each time-slice, so coefficients R_{ij}^x should be considered time dependant functions.

In a completely similar way, the coefficients R_{ij}^y , $i, j = 0, 1, 2$ can be defined. In addition, from the experimental data we have $R_{ii}^y \simeq R_{ii}^x$, $i, j = 0, 2$ so that

$$R_{00} = R_{11} + R_{22} + \frac{1}{P} \int_{t_0}^{t_0+\tau} \rho^2 |B_{00}^{(a)}|^2 dt, \quad (44)$$

where, for simplicity, we have omitted the superscripts x and y . It is interesting to note that R_{11} and R_{22} contain information specifically associated with ω_b and ω_a , respectively. The coefficient R_{00} , however, involves both frequencies.

Equations (18)–(22) now read

$$R_{01} = -\sqrt{2}R_{12}, \quad (45)$$

$$R_{02} = R_{20} = \frac{r}{2\sqrt{2}} \in \mathbb{R}, \quad (46)$$

$$a = R_{00} + 3R_{11} + 5R_{22}, \quad (47)$$

$$1 = R_{00} + R_{11} + R_{22}. \quad (48)$$

If mode a is assumed to remain stable throughout the pulse, from the above expressions and from the numerical data we would obtain $|r| < 0.42$, which does not agree with the experimental values. Thus we conclude that some evolution should exist along the pulse duration in the coefficients $B_{00}^{(a)}$, $B_{02}^{(a)}$ and $B_{20}^{(a)}$ associated to mode a (see Equation (35)).

Since

$$\frac{|r|}{2\sqrt{2}} \leq \sqrt{R_{00}R_{22}} \Rightarrow \sqrt{R_{22}} > \frac{|r|}{2\sqrt{2}\sqrt{R_{00}}} > \frac{|r|}{2\sqrt{2}}, \quad (49)$$

it follows from Equations (45)–(48) that

$$\frac{a}{2} - 0.9 < R_{11} < \frac{a-1}{2}, \quad (50)$$

$$\frac{r^2}{8} < R_{22} < \frac{a-1}{4}, \quad (51)$$

$$1.9 - \frac{r^2}{8} - \frac{a}{2} > R_{00} > \frac{3-a}{2}, \quad (52)$$

where, again, $a = s - r$, with s and r defined by Equations (23) and (24).

These inequalities provide bounds in the time-varying coefficients R_{ij} . In particular, for $t > 500$ ns, the experiments reveal that the spatial profile remains constant, and the inequalities (50)–(52) become

$$0.21 < R_{11} < 0.61, \quad (53)$$

$$0.13 < R_{22} < 0.30, \quad (54)$$

$$0.38 < R_{00} < 0.65, \quad (55)$$

$$R_{02} = R_{20} = -0.37. \quad (56)$$

Let us finally note that

$$\frac{1}{P} \int_{t_0}^{t_0+\tau} \rho^2 |B_{00}^{(a)}|^2 dt = R_{00} - R_{11} - R_{22}. \quad (57)$$

Accordingly, $R_{00} - R_{11} - R_{22}$ expresses the relative contribution of the product $\varphi_0(x)\varphi_0(y)$ at each time-slice. Furthermore, from the application of the experimental data to Equations (50)–(52) it follows that, in the interval $100 < t < 500$ ns, the weight of the bidimensional Gaussian function $\varphi_0(x)\varphi_0(y)$ decreases as the time increases. This confirms that, in the transition regime, mode b grows with respect to mode a.

4. Summary and conclusions

The time-resolved intensity profiles of TEA CO₂ laser pulses produced by low Fresnel number cavities have been investigated both analytically and experimentally. A simple scalar model has been introduced that represents the pulse amplitude as a linear combination of bidimensional H–G functions. According to this model, a number of general equations have been derived which relate the time-varying spatial structure to the second-order intensity moments at different times.

For the pulses analysed in the present work the following conclusions hold:

1. At the leading edge of the pulse ($t_0 < 100$ ns) there is only one mode, whose spatial structure can approximately be written as a superposition of the H–G functions $\varphi_0(x)\varphi_0(y)$, $\varphi_0(x)\varphi_2(y)$ and $\varphi_2(x)\varphi_0(y)$.
2. There is a transition interval ($100 < t_0 < 500$ ns) in which two modes are present. The spatial structure of the second mode exhibits two intensity lobes, which can be analytically represented as a linear combination of the

H-G functions $\varphi_0(x)\varphi_1(y)$ and $\varphi_1(x)\varphi_0(y)$. Depending on the relative phase factor between both functions, the lobes rotate.

3. At the rear edge of the pulse ($t_0 > 500$ ns), the beam profile reaches a doughnut-like spatial structure, although the central minimum is not zero. This structure is maintained nearly constant during the rest of the pulse. The doughnut shape comes from the second mode: when the phase difference between $\varphi_0(x)\varphi_1(y)$ and $\varphi_1(x)\varphi_0(y)$ is $\pi/2$, the mode intensity shows axial symmetry.

This behaviour can be understood by keeping in mind that the higher-order mode requires supplementary time to grow due to its stronger diffraction losses compared to those of the nearly Gaussian mode. This explains why after a large enough number of round trips (60–70 from the leading edge) the pulse reaches a nearly stationary spatial structure. Also note that the regions of the active medium filled by the two competing modes basically do not overlap.

It should be finally pointed out that, in a general case, when the number of transversal modes increases and the beam quality deteriorates ($M^2 > 2$), Equations (19)–(23) are not enough to infer the evolution of the detailed spatial structure of the pulsed beam from the measurements of the parameters $\langle x^2 \rangle$ and M^2 at each time-slice. This constitutes a limitation of the analytical model. Nevertheless, additional experimental data and supplementary hypothesis about the behaviour of the modes of the loaded cavity could overcome this difficulty. Also note that laser beams whose M^2 factor does not exceed, say, 2, are those that have most practical use.

Acknowledgment

The research work leading to this paper has been supported by the Comisión Interministerial de Ciencia y Tecnología of Spain, under Project PB97-0295, within the framework of EU-1269 Eureka Project.

References

- Bastiaans, M.J. *Optik* **82** 173, 1989.
- Caprara, A. and G.C. Reali. *Opt. Lett.* **17** 414, 1992.
- Chang, J.J. *Appl. Opt.* **33** 2255, 1994.
- Encinas-Sanz, F., J. Serna, C. Martínez, P.M. Mejías and R. Martínez-Herrero. *IEEE J. Quantum Electron.* **34** 1835, 1998.
- Gradshteyn, I.S. and I.M. Ryzhik. *Table of Integrals, Series and Products*, Academic Press, San Diego, 1980.
- Lavi, S., R. Prochaska and E. Keren. *Appl. Opt.* **27** 3696, 1988.
- Martínez, C., F. Encinas-Sanz, J. Serna, P.M. Mejías and R. Martínez-Herrero. *Opt. Commun.* **139** 299, 1997.

- Mejías, P.M. and R. Martínez-Herrero. *Opt. Lett.* **20** 660, 1995.
- Morin, M., M. Lebesque, A. Mailloux and P. Galarneau. *Proc. Soc. Photo-Opt. Instrum. Eng.* **2870** 206, 1996.
- Omatsu, T. and K. Kuroda. *Opt. Commun.* **87** 278, 1992.
- Perrone, M.R., C. Palma, V. Biagini, A. Piegari, D. Flori and S. Scaglione. *J. Opt. Soc. Am. A* **12** 991, 1995.
- Serna, J., R. Martínez-Herrero and P.M. Mejías. *J. Opt. Soc. Am. A* **8** 1094, 1991.
- Siegman, A.E. *Lasers*, University Science Books, Mill Valley, 1986.
- Siegman, A.E. *Proc. Soc. Photo-Opt. Instrum. Eng.* **1224** 2, 1990.
- Weber, H. *Opt. Quantum Electron.* **24** 1027, 1992.